

# Spatial clustering and halo occupation distribution modeling of local AGN via cross-correlation measurements with 2MASS galaxies

Mirko Krumpe,<sup>1\*</sup> Takamitsu Miyaji,<sup>2,3</sup> Alison L. Coil<sup>4</sup> and Hector Aceves<sup>2,3</sup>

<sup>1</sup>*Leibniz-Institut für Astrophysik Potsdam (AIP), An der Sternwarte 16, 14482 Potsdam, Germany*

<sup>2</sup>*IAUNAM-E (Instituto de Astronomía de la Universidad Nacional Autónoma de México Ensenada), Ensenada, Apdo. Postal 106, Ensenada BC, 22800 Mexico*

<sup>3</sup>*mailing address: IAUNAM-E (Instituto de Astronomía de la Universidad Nacional Autónoma de México Ensenada),*

*P.O. Box 439027, San Diego, CA 92143-9027, USA*

<sup>4</sup>*University of California, San Diego, Center for Astrophysics and Space Sciences, 9500 Gilman Drive, La Jolla, CA 92093-0424, USA*

Accepted 2017 October 13. Received 2017 October 12; in original form 2017 August 17

## ABSTRACT

We present the clustering properties and halo occupation distribution (HOD) modelling of very low redshift, hard X-ray-detected active galactic nuclei (AGN) using cross-correlation function measurements with Two-Micron All Sky Survey galaxies. Spanning a redshift range of  $0.007 < z < 0.037$ , with a median  $z = 0.024$ , we present a precise AGN clustering study of the most local AGN in the Universe. The AGN sample is drawn from the *SWIFT*/BAT 70-month and *INTEGRAL*/IBIS eight year all-sky X-ray surveys and contains both type I and type II AGN. We find a large-scale bias for the full AGN sample of  $b = 1.04^{+0.10}_{-0.11}$ , which corresponds to a typical host dark matter halo mass of  $M_h^{\text{typ}} = 12.84^{+0.22}_{-0.30} h^{-1} M_\odot$ . When split into low and high X-ray luminosity and type I and type II AGN subsamples, we detect no statistically significant differences in the large-scale bias parameters. However, there are differences in the small-scale clustering which are reflected in the full HOD model results. We find that low and high X-ray luminosity AGN, as well as type I and type II AGN, occupy dark matter haloes differently, with  $3.4\sigma$  and  $4.0\sigma$  differences in their mean halo masses, respectively, when split by luminosity and type. The latter finding contradicts a simple orientation-based AGN unification model. As a by-product of our cross-correlation approach, we also present the first HOD model of 2MASS galaxies.

**Key words:** galaxies: active – large-scale structure of the Universe – X-rays: galaxies

## 1 INTRODUCTION

Observed AGN clustering measurements as a function of AGN parameters such as redshift, luminosity, black hole mass, and accretion rate have received considerable interest in recent years (e.g. Coil et al. 2009; Shen et al. 2009; Mountrichas & Georgakakis 2012; Komiya et al. 2013; Koutoulidis et al. 2013; Zhang et al. 2013; Krumpe et al. 2015). These measurements not only provide access to the typical dark matter halo (DMH) mass in which AGN reside, but also constrain fundamental AGN physics when compared to different theoretical models of AGN triggering (e.g. Allevato et al. 2011). Instead of determining only a typical DMH mass, more recent clustering measurements are able to provide detailed constraints on how AGN popu-

late DMHs (see review Krumpe et al. 2014 and work by, e.g. Li et al. 2006; Mandelbaum et al. 2009; Padmanabhan et al. 2009; Shen et al. 2010; Miyaji et al. 2011) and thus reveal insights into how AGN are triggered and place them in a cosmological context.

Few studies exist of AGN clustering in the local Universe, as large-scale clustering measurements at very low redshift are challenging. First, the number density of AGN in the local Universe is an order of magnitude lower than at the peak of AGN activity at  $z \sim 2$  (e.g. Miyaji et al. 2015; Aird et al. 2015). Hence, there are substantially fewer AGN per unit comoving volume at low redshift compared to higher redshifts. Secondly, robust large-scale clustering measurements require surveys that span large cosmological volumes. At higher redshifts ( $z > 1$ ), surveys can provide this by covering only  $\sim 10 \text{ deg}^2$  on the sky. In the local Universe, however, only surveys that cover most of the sky can

\* E-mail: mkrumpe@aip.de

map a large enough comoving volume which also contains a sufficient number of AGN required for robust clustering measurements.

These issues make clustering measurements of local AGN extremely difficult, and only two studies of AGN clustering in the local Universe exist. Cappelluti et al. (2010) present the auto-correlation function (ACF) of 199 Seyfert AGN that are spectroscopically confirmed and detected by *Swift*/BAT in the 15–55 keV all-sky survey. The sample is drawn from Ajello et al. (2009) and covers a redshift range of  $0.001 \lesssim z \lesssim 0.15$  (with a median  $z = 0.045$ ). Due to the relatively low number of pair counts, Cappelluti et al. (2010) obtain correlation functions with large uncertainties.

Li et al. (2006) present the other study of AGN clustering in the local Universe. They use approximate 90 000 narrow-line AGN selected from SDSS data release 4. These optical type II AGN are extracted from the SDSS ‘main galaxy sample’ and have a median  $z = 0.10$ . Emission-line diagnostics (Kauffmann et al. 2003) are used to separate narrow-line AGN from galaxies in this study, for which the main emphasis is to compare the clustering of AGN to inactive galaxy samples with the same structural properties and stellar masses.

In this paper, we undertake an effort to compute the clustering properties of local AGN, as several recent improvements now allow more robust measurements and substantially tighter constraints on the halo occupation parameters of these AGN. The previous work of Cappelluti et al. (2010) is based on the 36-month *Swift*/BAT data. The latest available *Swift*/BAT all-sky hard X-ray survey uses 70 months of data (Baumgartner et al. 2013) and contains 553 spectroscopically classified Seyfert AGN. As hard X-rays are able to penetrate large amounts of obscuring material, a hard X-ray-selected-AGN sample has the great advantage of being almost unbiased with respect to the intrinsic absorbing column density of the central engine.

Additionally, Huchra et al. (2012) published the three-dimensional distribution of nearly 45 000 galaxies in the nearby Universe based on the Two-Micron All Sky Survey (2MASS; Skrutskie et al. 2006). This sample serves as a tracer set for the cross-correlation technique, which our team has used extensively in previous papers to study the clustering properties of broad-line AGN at redshifts of  $0.07 < z < 0.50$  (Krumpe et al. 2010 (paper I), Krumpe et al. 2012 (paper III), Krumpe et al. 2015 (paper IV)). Using cross-correlation measurements of AGN with a large number of galaxies in the same volume provides many more pairs (of galaxies and AGN) at all scales to use in the clustering measurements, compared to measuring only the ACF of AGN. In essence, the higher density of galaxies is used to more accurately trace the underlying cosmic web than can be achieved using only lower density AGN samples. Thus, the cross-correlation method used here is crucial to creating more robust AGN clustering measurements in the local Universe. This approach has been successfully used by other clustering studies as well (e.g. Li et al. 2006; Mandelbaum et al. 2009; Mountrichas & Georgakakis 2012).

In Miyaji et al. (2011) we present a theoretical method that allows us to determine the large-scale bias parameter directly from the measured cross-correlation function (CCF) between AGN and the galaxy tracer set, using halo occupation distribution (HOD) modelling. In Krumpe et al. (2012)

we show that this approach is strongly preferred over determining the bias parameter from a power-law fit of  $r_0$  and  $\gamma$  to the correlation function. Direct HOD modelling also allows us to constrain not only the large-scale bias for the AGN but also the full distribution of AGN in DMHs as a function of halo mass.

This paper is organized as follows. In Section 2 we describe the AGN data and samples and the 2MASS galaxy sample. Section 3 briefly summarizes the cross-correlation technique used here and how the HOD modelling is used to derive the AGN clustering properties. Section 4 shows the results of our clustering measurements. Our results are discussed in Section 5, and we present our conclusions in Section 6.

Determining the clustering properties of local AGN is of high interest to the astrophysical community. Powell et al. (submitted to ApJ) also initiated a study to explore local AGN clustering using a similar data set. As we do, they also make use of the cross-correlation technique using *Swift* BAT AGN and 2MASS galaxies, though they use a somewhat different sample selection criteria and methodology to analyse the correlation function.

Throughout this paper, all distances are measured in co-moving coordinates and given in units of  $h^{-1}$  Mpc, where  $h = H_0/100 \text{ km s}^{-1} \text{ Mpc}^{-1}$ , unless otherwise stated. We use a cosmology of  $\Omega_m = 0.3$ ,  $\Omega_\Lambda = 0.7$ , and  $\sigma_8(z = 0) = 0.8$ , which is consistent with the *Wilkinson Microwave Anisotropy Probe* data release 7 (Table 3 of Larson et al. 2011). We choose this set of cosmological parameters over more recent results from Planck (Planck Collaboration 2016) to be consistent with those used in our papers I–IV. Luminosities and absolute magnitudes are calculated using  $h = 0.7$ . We use AB magnitudes throughout the paper. All uncertainties represent  $1\sigma$  (68.3%) confidence intervals unless otherwise stated.

## 2 DATA

The galaxy sample used as our tracer set for the AGN-galaxy cross-correlation is based on the 2MASS redshift survey (Huchra et al. 2012). The AGN data are drawn from the 70-month *SWIFT*/BAT all-sky hard X-ray survey (Baumgartner et al. 2013) and the *INTEGRAL*/IBIS survey (Malizia et al. 2012, 2016). Here we provide relevant information on each of these samples.

### 2.1 2MASS Galaxies

The 2MASS (Skrutskie et al. 2006) mapped the entire sky in the  $J$ ,  $H$ , and  $K_S$  bands using twin 1.3-m telescopes located at Mount Hopkins, AZ and Cerro Tololo, Chile from 1997–2001. 2MASS contains 470 million sources, out of which 1.6 million are extended. Jarrett (2004) present an extended source photometric catalogue of approximately 1 million objects with  $K_S \leq 13.5$  mag. This catalogue constitutes the initial selection of sources for the redshift survey.

The primary extragalactic goal of the 2MASS was the generation of an all-sky galaxy redshift survey, to map the large-scale structure of the local Universe. Thus, a spectroscopic program was undertaken with the goal of observing all objects with (i)  $K_S \leq 11.75$  mag and detected at  $H$ , (ii)

$E(B - V) \leq 1$  mag, and (iii)  $|b| \geq 5^\circ$  for  $30^\circ \leq l \leq 330^\circ$ ;  $|b| \geq 8^\circ$  otherwise. The latter is used to avoid confusion near the galactic plane and galactic centre, respectively. The 2MASS magnitudes are extinction corrected. Huchra et al. (2012) present the redshifts for 43 533 galaxies (97.6%) out of 44 599 entries that match the aforementioned criteria. The redshifts are taken from various sources (e.g. Sloan Digital Sky Survey DR8; 6dF Galaxy Survey DR3; NASA Extragalactic Database), including spectroscopic follow-up observations conducted between 1998–2011.

The galaxies within the 2MASS redshift survey span all morphological types (elliptical, spiral, irregular, unbarred, barred, etc.). Spirals dominate the sample at  $z < 0.03$ , while ellipticals dominate at higher redshifts. Unfortunately, morphological classifications exist for only 20 860 galaxies with  $K_S \leq 11.25$  or fainter if the morphological types were available from the literature. Thus, for the entire 2MASS galaxy redshift sample it is not possible to select a galaxy subsample based uniformly on morphological classification.

### 2.1.1 2MASS Galaxy Sample

For our 2MASS galaxy sample, we select all 2MASS redshift survey galaxies with  $|b| \geq 8^\circ$  and within a redshift range of  $0.007 \leq z \leq 0.037$ . We compute absolute  $K_S$  magnitudes ( $M_{K_S}$ ) based on the total extinction-corrected magnitude. Since galaxy clustering is known to depend on luminosity (e.g. Zehavi et al. 2011), we create a volume-limited sample by selecting only galaxies with  $-24.4 \leq M_{K_S} \leq -25.9$  (Fig. 1). This selection ensures that the clustering of the galaxies used in this paper as the tracer set remains constant over the redshift range used here. This absolute magnitude limit results in a tracer sample that is restricted to  $z \leq 0.037$ .

In the process of performing the analyses for this paper, we initially used multiple redshift ranges. We initially split the galaxy sample into low- and high-redshift subsamples and computed the ACFs of these subsamples. We noticed that including galaxies with redshifts above  $\sim 0.04$  leads to increasingly different clustering properties between the low and high-redshift subsamples. This is due to the ratio of spirals to ellipticals dropping substantially above  $z \sim 0.04$ , reflecting the increased fraction of elliptical galaxies leading to a higher clustering signal. Because morphological types are only available for approximately half of the galaxy sample, it is not possible to create subsamples that contain only spiral or elliptical galaxies and hence overcome this issue.

The final redshift range used here is a trade-off between (i) maximizing the number of possible cross-correlated pairs between 2MASS galaxies and AGN, and (ii) identifying a redshift range in which the 2MASS galaxies show little to no evolution of the large-scale bias parameter as a function of redshift. At  $z \lesssim 0.037$  the fraction of spiral and elliptical galaxies is roughly constant (maximal derivation from the median value  $\pm 8\%$ ), which results in very similar clustering amplitudes in the low and high-redshift subsamples (for details see Section 4.1). This is crucial for our study, as here we use the CCF with the tracer sample across the full redshift range of  $0.007 \leq z \leq 0.037$  to decrease the error bars, and this approach relies on the galaxy tracer set clustering properties not evolving strongly over the full redshift range used. We therefore strongly recommend that the 2MASS galaxy

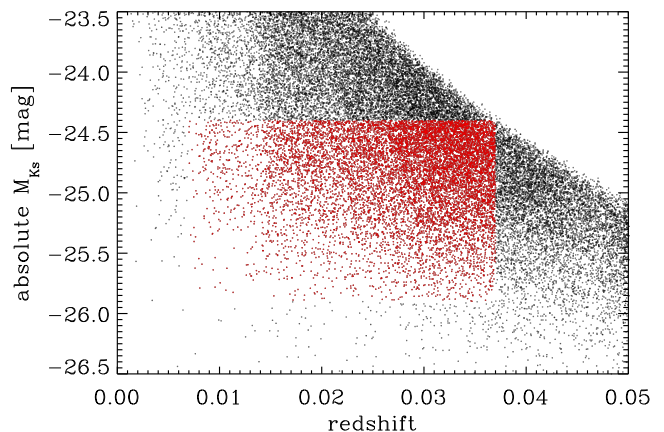


**Figure 1.** Absolute  $K_S$  magnitude versus redshift for galaxies in the 2MASS redshift survey (black). Galaxies in red indicate our tracer sample of 10 900 galaxies used for cross-correlation measurements with  $0.007 \leq z \leq 0.037$  and  $-24.4 \leq M_{K_S} \leq -25.9$ .

sample above  $z \sim 0.4$  not be used for cross-correlation studies, unless one is willing to accept significantly increased systematic errors.

The depth of 2MASS depends on variations in, for example, the seeing and sky background. The magnitude limits are therefore selected such that the source sensitivity and detection are complete under all observing conditions for the survey. Consequently, no spatial window function is required. Within and around the Magellanic clouds, we recognize no significant excess or deficit in number density of 2MASS sources with  $K_S \leq 11.75$  mag. Thus, areas covered by the Magellanic clouds are included. The final sample contains 10 900 objects covering  $35\,512\text{ deg}^2$  of the sky. The number density of the volume-limited sample used here is  $n = (2.29 \pm 0.13) \times 10^{-3} h^3 \text{ Mpc}^{-3}$ .

To estimate the uncertainties in the number density and the clustering amplitude (see Section 3.2), we divide the survey area into 22 subsections of  $\sim 1500\text{--}1850\text{ deg}^2$  each. The decision to create relatively large subsections and therefore a moderate number of jackknife samples is based on the largest scales that we aim to probe with our clustering measurements. The final 2MASS sample covers a redshift range of  $0.007 \leq z \leq 0.037$ , with a median redshift of  $\langle z \rangle = 0.029$ . We measure the correlation function to a projected distance of  $30 h^{-1} \text{ Mpc}$ . The angular distance of  $30 h^{-1} \text{ Mpc}$  at a redshift of  $z = 0.01$  corresponds to  $\sim 40^\circ$ . Thus to include this scale in each jackknife subsection,  $\sim 1600\text{ deg}^2$  are required for each subsection.

### 2.1.2 2MASS Random Sample

In order to compute the correlation function, a random galaxy sample is required (see Section 3.1 below). Since no spatial window function is needed for the observed 2MASS galaxy sample, we randomly distribute objects on the sky. We select only those sources with  $|b| \geq 8^\circ$  to match the observed sample. The random catalogue contains 500 times the number of 2MASS galaxies in our tracer set. This ensures that we minimize the uncertainties introduced due to

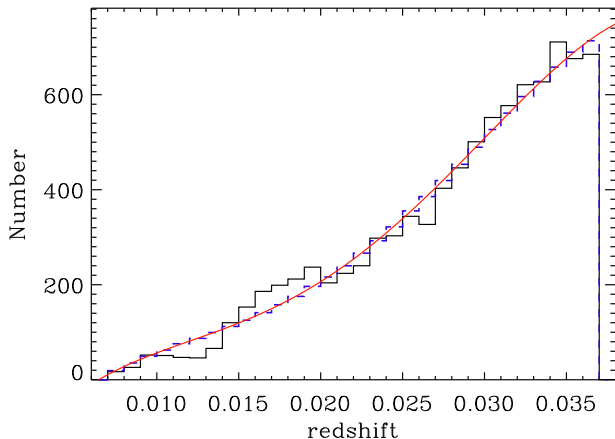


**Figure 2.** Redshift histogram for the observed 2MASS galaxy sample used as our tracer set (black histogram), the smoothed redshift profile (smooth red solid line) and the random sample (blue-dashed, renormalized to the distribution of 2MASS galaxies).

statistical effects of the random catalogue, even for pairs at the smallest scales measured here.

The corresponding redshift for a random object is randomly chosen from the smooth redshift distribution of the 2MASS galaxy sample tracer set (Fig. 2). The smoothing applies a least-squares (Savitzky & Golay 1964) low-pass filter to the observed 2MASS redshift distribution.

## 2.2 *SWIFT*/BAT AGN

The *SWIFT* gamma-ray burst observatory (Gehrels et al. 2004) has continuously observed the hard X-ray sky with the Burst Alert Telescope (BAT) in an energy range of 14–195 keV since its launch in 2004. The BAT is a coded-mask telescope with a field of view of  $\sim 60^\circ \times 100^\circ$ . The effectively random pointing strategy developed to detect and study gamma-ray bursts is also well suited for performing an all-sky survey with uniform sky coverage. Due to its large field of view, BAT covers approximately one-sixth of the sky with each pointing.

As the total observation time accumulates higher sensitivity is reached, which combined with an improved data reduction pipeline results in more detected sources. In eight-band mosaics, sources are determined by identifying  $4.8\sigma$  events, compared to their surrounding neighbours. The sources are then cross-correlated with archival X-ray images from high-resolution instruments and extended objects in the 2MASS all-sky survey. The flux of known bright sources, which are detected with a significance greater than  $6\sigma$ , are subtracted and the source detection is performed on the resulting cleaned images. This survey is the most sensitive hard X-ray all-sky survey in existence and reaches a flux of  $1.3 \times 10^{-11} \text{ erg s}^{-1} \text{ cm}^{-2}$  over 90% of the sky (14–195 keV band). A detailed description on the 70-month *SWIFT*/BAT all-sky hard X-ray survey can be found in Baumgartner et al. (2013).

NED and SIMBAD are used to determine the source type and redshift of the counterparts. Almost 60% of the 70-month *SWIFT*/BAT all-sky hard X-ray survey classi-

cations are AGN. Baumgartner et al. (2013) list subtypes of AGN such as Seyfert I (Sy1.0–1.5), Seyfert II (Sy1.7–2.0) and QSOs (luminosities larger than  $10^{45} \text{ erg s}^{-1}$ ). For all these sources the 14–195 keV luminosities as well as their photon indices (based on a fit to the eight-channel spectra) are provided.

## 2.3 *INTEGRAL*/IBIS AGN

The Imager on Board the *INTEGRAL* Satellite (IBIS) also provides an all-sky hard X-ray source catalogue. This coded mask instrument with an energy range of 15 keV – 10 MeV features higher angular resolution ( $\sim 12 \text{ arcmin}$ , FWHM) compared to the  $\sim 20 \text{ arcmin}$  resolution of *SWIFT*/BAT. Bird et al. (2016) published the *INTEGRAL*/IBIS all-sky hard X-ray source catalogue of all the data publicly available starting from the 12th orbit of *INTEGRAL* (end of 2002) up to the end of 2010.

Malizia et al. (2012, 2016) present several hundred AGN detected by *INTEGRAL*, for which they also provide the optical classification, redshift, X-ray column density measurements and 20–100 keV luminosities. The counterpart classification uses literature and NED searches, as well as their own follow-up spectroscopy. The AGN are further distinguished into Sy1, Sy1.2, Sy 1.5, Sy1.9, Sy2 and QSO. In their 2016 paper they list additional objects since 2010 and only for those they also provide the photon index. The primary goal of this survey is to study the absorption properties in a large sample of hard X-ray selected, and thus unbiased, AGN sample. For more details on the *INTEGRAL*/IBIS AGN catalogues see Malizia et al. (2012, 2016).

## 2.4 Combined *SWIFT*/*INTEGRAL* AGN Sample

In order to maximize the number of hard X-ray-selected AGN to use for our clustering measurements, we combine the 70-month *SWIFT*/BAT AGN and the *INTEGRAL*/IBIS AGN catalogues. This is possible as both samples cover a similar parameter space in redshift, luminosity, column density, and photon index.

Only AGN within a redshift range of  $0.007 \leq z \leq 0.037$ , matching our 2MASS galaxy redshift range, are considered. Furthermore, an object is only included if  $|b| \geq 8^\circ$ . We begin with the *SWIFT*/BAT AGN sample, which in this redshift range contains 112 type I and 141 type II AGN. We then identify additional *INTEGRAL* AGN from the 2012 and 2016 catalogues that are not included in the 70-month *SWIFT*/BAT AGN sample. Identical to the *SWIFT*/BAT source classification, *INTEGRAL* subclassifications of Sy1.0–1.5 and Sy1.9–2.0 are classified as type I and type II AGN, respectively. QSOs are included in the type I samples for both *SWIFT* and *INTEGRAL*. The 2012 *INTEGRAL* AGN catalogue adds one additional type I and eight type II AGN to our AGN sample. The 2016 *INTEGRAL* AGN catalogue adds an additional eight unique type II AGN. Thus, the final sample contains 274 AGN (including four *SWIFT* AGN with the classification “other AGN”, but excluding blazar/BL Lac objects) of which 113 and 157 are type I and type II AGN, respectively.

Figs. 3–5 show the redshift and luminosity distributions



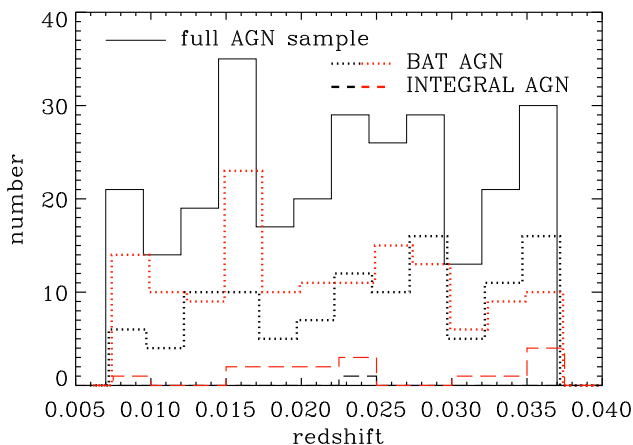


**Figure 3.** Redshift histogram of the full AGN sample (black solid line), divided into subsamples based on the catalogue used for identification (dotted line – *SWIFT*/BAT, dashed line – *INTEGRAL*/IBIS) and AGN type classification (black – type I AGN, red – type II AGN). For clarity, we slightly shift the redshift values of the BAT and *INTEGRAL* subsamples in the histogram.

of the full AGN sample, divided into type I and type II subsamples. Although subject to low number statistics, the full, type I, and type II AGN samples have similar redshift and luminosity distributions. We convert the 20–100 keV *INTEGRAL* luminosities into the 14–195 keV *SWIFT* energy band by multiplying the 20–100 keV *INTEGRAL* luminosity with a factor of 1.65. This value was determined from WebPIMMS<sup>1</sup>, using a median *SWIFT* AGN photon index of 1.93.

We check whether the same AGN received identical *SWIFT* and *INTEGRAL* type classifications. Out of 82 AGN in common between the *SWIFT* AGN sample and the *INTEGRAL* 2012 AGN sample, 78 agree in their AGN classifications. Additionally, Fig. 6 shows that there is no degeneracy between X-ray luminosity and column density for the AGN in our sample.

Depending on its sky position, we assign each AGN to a corresponding jackknife subsection. This procedure is identical to the one used for the 2MASS galaxy sample (see Section 2.1.1). The selected 2MASS galaxy sample and the AGN sample have 113 objects in common. The distribution of the finally selected 2MASS galaxy sample and hard X-ray-selected AGN are shown in Fig. 7.

## 2.5 Black hole mass estimates

Koss et al. (2017) present black hole mass estimates for a subset of AGN detected in the *SWIFT*/BAT 70-Month catalogue. For 201 objects (31% of the complete *SWIFT*/BAT AGN sample), these estimates are derived from stellar velocity dispersion measurements. For 227 objects the estimates are single-epoch virial black hole masses derived from broad emission lines. In total 415 unique objects have black hole

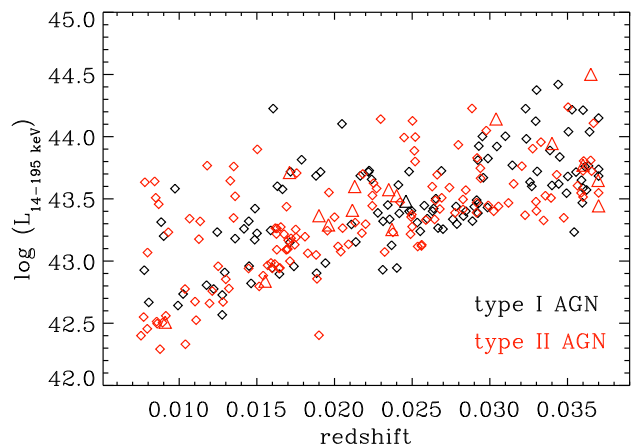


**Figure 4.** X-ray luminosity versus redshift for the full AGN sample. The different symbols and colours represent the different catalogues used for identification and the AGN classification types: diamonds – *SWIFT*/BAT, triangles – *INTEGRAL*/IBIS, black – type I AGN and red – type II AGN.

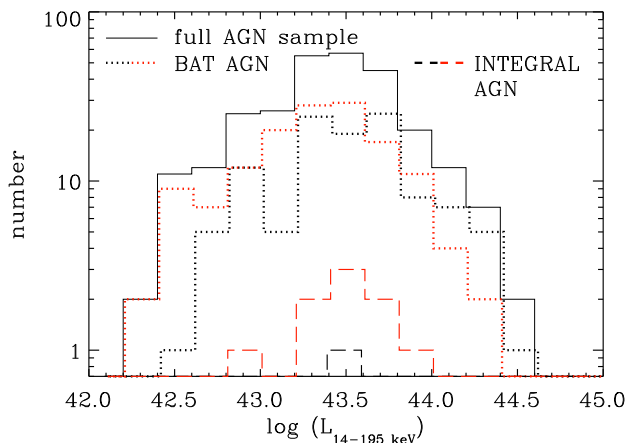


**Figure 5.** X-ray luminosity histogram of the full AGN sample (black solid line) and subsamples based on identification catalogue and AGN classification type. Line types and colours are identical to Fig. 3.

mass estimates from one or both of these techniques. Applying our redshift cuts and restricting to  $|b| \geq 8^\circ$  for the complete *SWIFT*/BAT AGN sample, 181 objects out of 274 in total have black hole mass estimates (119 from stellar velocity dispersion measurements, 69 from single epoch spectroscopy and 7 from both methods). We remove 11 sources that have disagreement between BASS and the 70-month *SWIFT*/BAT AGN catalogue. According to the latter these sources are not classified as AGN.

In our redshift range, Fig. 8 demonstrates that black hole masses based on stellar velocity dispersion have, on average, substantially higher masses than estimates from single-epoch spectra. For the seven objects that have mass estimates from both methods, the masses derived using stellar velocity dispersion are on average 0.8 dex higher than those based on single-epoch spectroscopy.

<sup>1</sup> <https://heasarc.gsfc.nasa.gov/cgi-bin/Tools/w3pimms/w3pimms.pl>

Based on work by Koji Mukai, Michael Arida and Ed Sabol

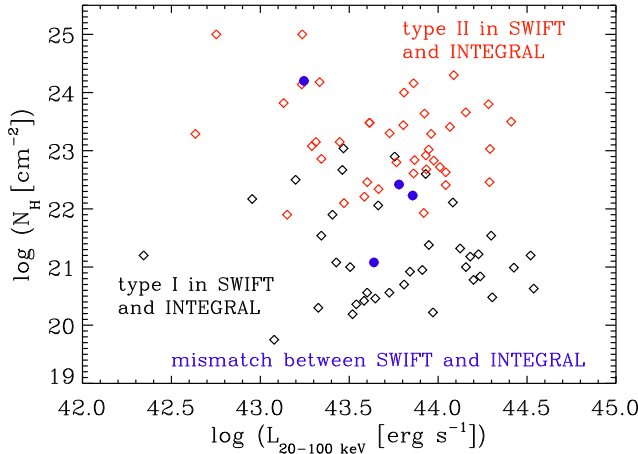


**Figure 6.** X-ray luminosity in the 20–100 keV band versus intrinsic column density  $N_H$  for AGN that fulfil our selection criteria and are found in both the *SWIFT* and *INTEGRAL* 2012 catalogues. Black (type I) and red (type II) open symbols represent those sources that have the same AGN subclass in each catalogue. Filled blue circles show sources that have different classifications in the two catalogues.

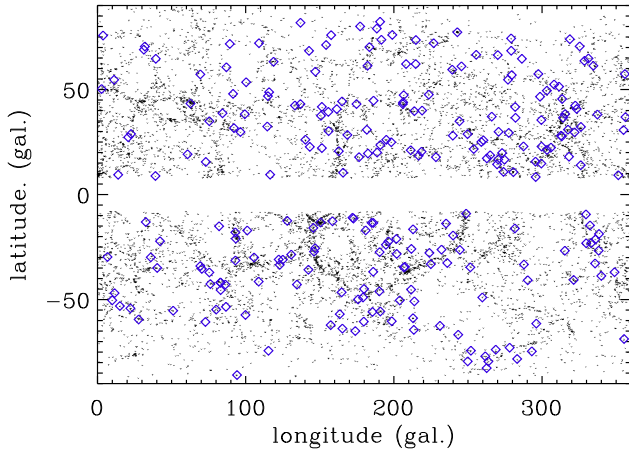


**Figure 7.** Distribution in galactic coordinates of the 10 900 2MASS galaxies in the tracer set (black dots) and 274 AGN selected using *SWIFT* and *INTEGRAL* catalogues (blue diamonds). Note the restriction of  $|b| \geq 8^\circ$  for both, the 2MASS galaxy sample and the AGN sample.

## 2.6 AGN subsamples

In addition to the full AGN sample, which contains 274 sources, we also create subsamples according to different available AGN parameters (see Table 1).

First, we split the full AGN sample at the median X-ray luminosity of  $\log(L_{14–195 \text{ keV}} / [\text{erg s}^{-1}]) = 43.42$ . The median  $\log L_X$  between the low- and high- $L_X$  samples differs by 0.5 dex. Comparing the sources for which a photon index is available, the median photon indices of both samples are very similar. The fractions of type I and type II objects in each sample are slightly different (low- $L_X$  AGN: 36% type I, 64% type II; high- $L_X$  AGN: 47% type I, 53% type II).

Secondly, we select the 170 objects classified as AGN

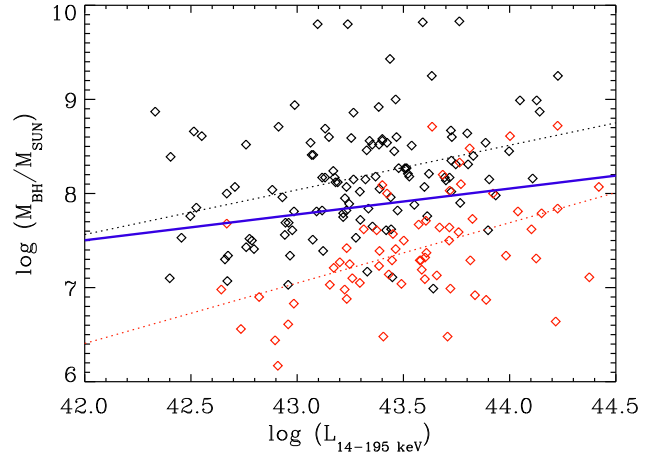


**Figure 8.** Black hole mass estimates from Koss et al. (2017) versus X-ray luminosity for AGN in the 70-month *SWIFT*/BAT catalogue. Black data points show mass estimates derived from stellar velocity dispersion measurements, while red data points show estimates derived from single epoch spectroscopy. The corresponding  $\chi^2$  minimization linear fits are shown as black and red dotted lines. The linear fit of the combined sample is shown as a blue solid line.

in Baumgartner et al. (2013) for which black hole mass estimates are available from Koss et al. (2017). We split the resulting sample at the median black hole mass of  $\log(M_{BH}/M_\odot) = 7.88$ . The low and high black hole mass samples contain 86 and 84 objects, respectively. The median black hole masses and redshifts of these samples are  $\log(M_{BH,low}/M_\odot) = 7.39$  and  $\log(M_{BH,high}/M_\odot) = 8.39$  and  $\langle z_{low} \rangle = 0.022$  and  $\langle z_{high} \rangle = 0.026$ . The low- $M_{BH}$  sample contains 50 type I and 35 type II AGN, with the remaining three classified as ‘other AGN’. The high- $M_{BH}$  sample contains 27 type I and 56 type II AGN, with one ‘other’ AGN.

Thirdly, we split into type I and type II AGN classification (113 sources are in the type I sample, 157 sources are in the type II sample). The samples have median X-ray luminosities of  $\log(L_{14–195 \text{ keV}} / [\text{erg s}^{-1}]) = 43.45$  and 43.36 for the type I and type II samples, respectively, with corresponding photon indices of 2.01 and 1.85. Fig. 6 illustrates that a split into type I and type II subsamples is very similar to a split in intrinsic column density  $N_H$ . Since we do not have  $N_H$  for all sources, we consider the results splitting into type I and type II as an estimate for the clustering dependence on  $N_H$  below.

Fourthly, we split the sample with respect to a photon index of  $\Gamma = 1.93$ . For these subsamples, we use only the *SWIFT* and *INTEGRAL* 2016 AGN catalogues, as only these catalogues contain photon indices. The low- and high- $\Gamma$  samples have median photon indices of  $\Gamma_{low} = 1.76$  and  $\Gamma_{high} = 2.07$ . The corresponding X-ray luminosities are very similar, but the fractions of type I and type II AGN in each sample are quite different (low- $\Gamma$  AGN: 28% type I, 72% type II; high- $\Gamma$  AGN: 60% type I, 40% type II).

### 3 METHODOLOGY

#### 3.1 Cross-correlation clustering measurements

We follow the same methodology as described in Section 4 of Papers III and IV and repeat the salient features here. We measure the two-point correlation function  $\xi(r)$  (Peebles 1980), which measures the excess probability  $dP$  of finding an object in a volume element  $dV$  at a distance  $r$  from another randomly chosen object. The ACF measures the spatial clustering of objects in the same sample, while the CCF measures the clustering of objects in two different samples. We determine the ACF of the 2MASS galaxy sample and the CCF between the AGN sample (and subsamples) with 2MASS galaxies.

For both types of correlation functions, we use the correlation estimator of Davis & Peebles (1983) in the form

$$\xi(r) = \frac{DD(r)}{DR(r)} - 1, \quad (1)$$

where  $DD(r)$  is the number of data-data pairs with a separation  $r$  and  $DR(r)$  is the number data-random pairs. Both pair counts have been normalized by the number density of data and random points. This simple estimator has several major advantages and results in only a marginal loss in the S/N when compared to more advanced estimators (e.g., Landy & Szalay 1993). The estimator requires the generation of a random catalogue only for the tracer set. The selection effects of the AGN sample, including possible non-uniformity of the flux-limit of the catalogue, are extremely difficult to model. Thus, accepting a marginal loss in the signal-to-noise (S/N) leads to the greater benefit of smaller systematic uncertainties due to the lack of the requirement of modelling the very complex AGN selection function.

To separate the effect of redshift distortions, the correlation function is measured as a function of two components of the separation vector between two objects, i.e., one perpendicular to ( $r_p$ ) and the other along ( $\pi$ ) the line of sight.  $\xi(r_p, \pi)$  is thus extracted by counting pairs on a two-dimensional grid of separations  $r_p$  and  $\pi$ . We obtain the projected correlation function  $w_p(r_p)$  by integrating  $\xi(r_p, \pi)$  along the  $\pi$  direction.

We measure  $r_p$  in the range of  $0.05\text{--}30\ h^{-1}\text{ Mpc}$  in 14 logarithmic bins. We compute  $\pi$  in steps of  $5\ h^{-1}\text{ Mpc}$  in the range  $\pi = 0\text{--}200\ h^{-1}\text{ Mpc}$ . To derive  $\pi_{\max}$ , we compute  $w_p(r_p)$  for a set of  $\pi_{\max}$  ranging from 10 to 160  $h^{-1}\text{ Mpc}$  in steps of  $10\ h^{-1}\text{ Mpc}$ . We then fit  $w_p(r_p)$  for  $r_p = 0.3\text{--}30\ h^{-1}\text{ Mpc}$ , using a fixed  $\gamma = 1.9$ , and determine the correlation length  $r_0$  for the individual  $\pi_{\max}$  measurements using the following equation:

$$w_p(r_p) = r_p \left( \frac{r_0}{r_p} \right)^\gamma \frac{\Gamma(1/2)\Gamma((\gamma-1)/2)}{\Gamma(\gamma/2)}. \quad (2)$$

For the 2MASS galaxy ACF and the AGN–2MASS CCFs the  $r_0$  signal has already saturated at  $\pi_{\max} = 40\ h^{-1}\text{ Mpc}$ . For larger values of  $\pi_{\max}$  the corresponding correlation lengths do not change by more than  $1\sigma$ , and the uncertainties increase with increasing  $\pi_{\max}$  values.

#### 3.2 Error Analysis

The error analysis is also identical to Papers I, III and IV. We use the jackknife resampling technique to estimate the

measurement errors based on the covariance matrix  $M_{ij}$ , which reflects the degree to which bin  $i$  is correlated with bin  $j$ .

As discussed above in Section 2.1.1, we divide the survey area into  $N_T = 22$  subsections, determined such that each subarea spans the largest scale studied in this paper. The  $N_T$  jackknife-resampled correlation functions define the covariance matrix:

$$M_{ij} = \frac{N_T - 1}{N_T} \left[ \sum_{k=1}^{N_T} \left( w_k(r_{p,i}) - \langle w(r_{p,i}) \rangle \right) \times \left( w_k(r_{p,j}) - \langle w(r_{p,j}) \rangle \right) \right] \quad (3)$$

We calculate  $w_p(r_p)$   $N_T$  times, where each jackknife sample excludes one section,  $w_k(r_{p,i})$  and  $w_k(r_{p,j})$  are from the  $k$ th jackknife samples of the AGN ACF and  $\langle w(r_{p,i}) \rangle$  and  $\langle w(r_{p,j}) \rangle$  are the averages over all of the jackknife samples. The uncertainties represent  $1\sigma$  (68.3%) confidence intervals ( $\sigma_i = \sqrt{M_{ii}}$ ).

#### 3.3 HOD modelling

We interpret our results using HOD modelling, following an approach similar to that presented in paper II. We use the HOD approach to obtain linear bias parameters as well as to investigate differences in the measured CCFs among various subsamples of the *Swift* BAT/Integral IBIS AGN with 2MASS galaxies beyond differences in the bias parameters alone. In this paper we do not intend to present full constraints of the AGN HODs. Thus the HOD model of the AGN is deliberately made simple.

The outline of our approach is as follows:

(i) We first apply the HOD modelling technique to the ACF of the 2MASS galaxies and find accurate central and satellite HODs using a correlated  $\chi^2$  fit with a four free parameter model. The number density constraint is also included. The best-fitting parameter search is made with a Markov chain Monte Carlo (MCMC) method.

(ii) In order to model the CCF between the 2MASS galaxies and AGN, two sets of HODs are needed, the HOD of the 2MASS galaxies derived in the previous step and that of the AGN. Since the 2MASS galaxy sample size is much larger than that of those of the AGN samples, and therefore the statistical significance of the 2MASS galaxy ACF is much better than that of the 2MASS galaxy–AGN CCF, we use the best-fitting 2MASS galaxy HOD derived above and a very simplified two free parameter HOD model for the AGN.

(iii) By performing a correlated  $\chi^2$  fit to the CCF, we constrain the two free parameters for the AGN HOD. HOD modelling of the 2MASS ACF and the 2MASS galaxy–AGN CCF is performed on scales of  $0.05 \leq r_p \leq 30\ h^{-1}\text{ Mpc}$ . For the CCF AGN subsamples we impose a minimum  $r_p$  such that the number of pairs in the bins used for the fit have at least 16 pairs, in order to apply robust  $\chi^2$  statistics.

For consistency with our previous papers, we use the bias parameter as a function of halo mass relation of Tinker et al. (2005) and the halo mass function of Sheth et al. (2001) in our HOD modelling. A number of improvements have been made to our HOD modelling since

paper II. We use the software **camb**<sup>2</sup> (by Anthony Lewis and Anthony Challinor) to generate the linear power spectrum for the cosmological parameters specified in Section 1. The effects of halo–halo collision and scale-dependent bias to the two-halo term described in appendix B of (Tinker et al. 2005) are fully included.

This removes the need to ignore the results in the  $r_p$  range around the transition between one-halo and two-halo dominated regimes (see paper II). Instead of using equation (7) of paper II, where  $w_p(r_p)$  for one- and two-halo terms are transformed from the respective model power spectra through the zeroth-order Bessel function of the first kind, here we use

$$\begin{aligned} w_{p,1h}(r_p) &= 2 \int_0^{\pi_{\max}} [1 + \xi_{1h}(r_p, \pi)] d\pi. \\ w_{p,2h}(r_p) &= 2 \int_0^{\pi_{\max}} \xi_{2h}(r_p, \pi) d\pi. \end{aligned} \quad (4)$$

Hereafter, the quantities for AGN are represented by a subscript ‘A’, 2MASS galaxies by ‘G’ (representing *galaxies*), and CCF between the two by ‘AG’. We denote the galaxy HODs at the halo centre and of satellites by  $\langle N_{G,c} \rangle(M_h)$  and  $\langle N_{G,s} \rangle(M_h)$ , respectively. Now  $\langle N_G \rangle(M_h) = \langle N_{G,c} \rangle(M_h) + \langle N_{G,s} \rangle(M_h)$ . Likewise, the HODs of the AGN at the halo centres, of satellites, and the sum of the two are denoted by  $\langle N_{A,c} \rangle(M_h)$ ,  $\langle N_{A,s} \rangle(M_h)$  and  $\langle N_A \rangle(M_h)$ .

### 3.3.1 HOD of 2MASS Galaxies

For the HOD modelling of the 2MASS galaxy sample, we use the five parameter model of Zheng et al. (2007):

$$\begin{aligned} \langle N_{G,c} \rangle(M_h) &= \frac{1}{2} \left[ 1 + \operatorname{erf} \left( \frac{\log M_h - \log M_{\min}}{\sigma_{\log M}} \right) \right] \\ \langle N_{G,s} \rangle(M_h) &= \langle N_{G,c} \rangle(M_h) \left( \frac{M_h - M_0}{M'_1} \right)^{\alpha_s}, \end{aligned} \quad (5)$$

where the five model parameters are  $M_{\min}$ ,  $\sigma_{\log M}$ ,  $M_0$ ,  $M'_1$ , and  $\alpha_s$ . HOD studies on various galaxy samples by Zehavi et al. (2011) show  $M_{\min} \approx M_0$  and  $M_0$  becomes poorly constrained when it is allowed to vary freely (Skibba et al. 2015). Thus, we impose  $M_{\min} = M_0$ .

Best fitting parameters are searched for by minimizing correlated  $\chi^2$ :

$$\begin{aligned} \chi^2 &= \sum_{ij} \{ [w_p(r_{p,i}) - w_p^{\text{mdl}}(r_{p,i})] M_{ij}^{-1} \times \\ &\quad [w_p(r_{p,j}) - w_p^{\text{mdl}}(r_{p,j})] \} + \\ &\quad (n_G - n_G^{\text{mdl}})^2 / \sigma_{n_G}^2, \end{aligned} \quad (6)$$

where the quantities from the model are indicated by a superscript ‘mdl’,  $M_{ij}$  is the covariance matrix (equation 3),  $n_G$  the number density of 2MASS galaxies and  $\sigma_{n_G}$  is its  $1\sigma$  error respectively. We measure  $n_G = (2.29 \pm 0.13) \times 10^{-3} h^3 \text{Mpc}^{-3}$ , where the  $1\sigma$  error is estimated by jackknife resampling.

The best-fitting parameter search is made using an MCMC method with the MCMC-F90 library of Marko Laine<sup>3</sup>, which has been linked to our HOD model calculation software.

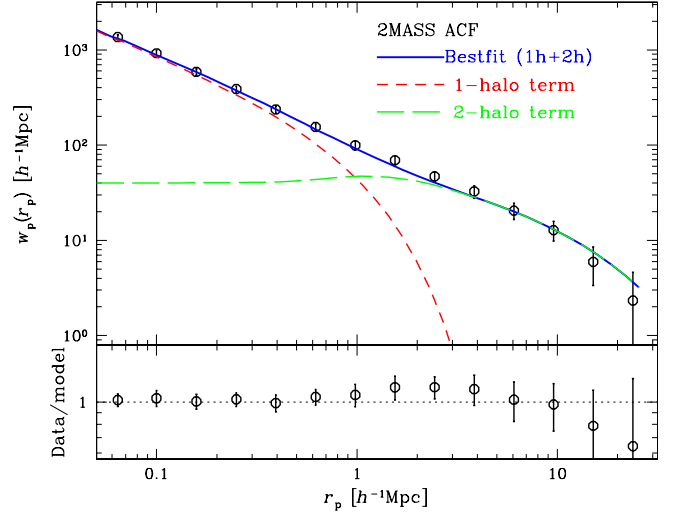


**Figure 9.** The 2MASS galaxy ACF (black circles) with  $1\sigma$  error bars is shown with the best-fitting HOD model (blue solid line). The one-halo and two-halo terms of the HOD model are also shown in red short dashed and green long dashed lines, respectively. The lower panel shows the fit residuals in terms of the data/model ratio.

### 3.3.2 HOD of Swift BAT AGN Samples

We fit HOD models to the CCFs between the 2MASS galaxy and the AGN (sub)samples. To calculate the expected CCF  $w_p(r_p)$ , we use the best-fitting HOD of the 2MASS galaxies derived above and a parametrized model of the AGN HOD. Because the AGN sample size is much smaller than the 2MASS sample size, the HOD of the 2MASS galaxies is fixed to the best-fitting values from the ACF. As discussed above, we use a very simple HOD model for the AGN samples, of the form

$$\begin{aligned} \langle N_{A,c} \rangle &= f_A \Theta(M_h - M_{\min}), \\ \langle N_{A,s} \rangle &= f_A \Theta(M_h - M_{\min}) [(M_h - M_0)/M'_1]^{\alpha_s}, \end{aligned} \quad (7)$$

where  $f_A$  is the AGN fraction (duty cycle) among central galaxies at  $M_h \gtrsim M_{\min}$  and  $\Theta(x)$  is a step function that has the value of 0 at  $x < 0$  and 1 at  $x \geq 0$  respectively. Like the case of the galaxy ACF, we set  $M_0 = M_{\min}$ . Note that this is essentially the same model as model B of paper II except that here we use  $M_0 = M_{\min}$  rather than zero. Furthermore, we set  $M'_1/M_{\min} = 10$ , which approximately represents the HODs of most luminosity-threshold nearby galaxy samples (Section 3.3.1; Zehavi et al. 2011). We do not use AGN density constraints, and the value of  $f_A$ , which is the global normalization of the AGN HOD, does not affect the resulting CCF. Thus our free parameters are  $\log M_{\min}$  and  $\alpha_s$ .

We search for best-fitting values and confidence ranges by calculating  $\chi^2$  using parameter grids spanning  $9.8 \leq \log M_{\min}[h^{-1}M_\odot] \leq 13.6$  and  $-0.6 \leq \alpha_s \leq 1.29$ . The upper bounds for both parameters are chosen such that the parameter region accommodates  $\Delta\chi^2 = 4.6$  for all subsamples. The lower bound of  $\log M_{\min}$  is imposed as below this minimum mass the analytical  $b(M_h)$  relation flattens or even

<sup>2</sup> <http://camb.info/>

<sup>3</sup> <http://helios.fmi.fi/~lainema/mcmcf90/>



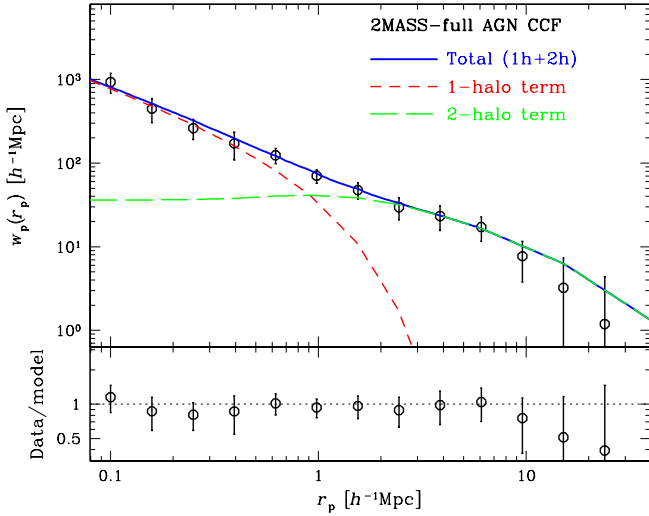


**Figure 10.** The measured CCF between 2MASS galaxies and the full AGN sample, shown with the best-fitting HOD model and fit residuals displayed as data/model. The symbols and line styles have the same meanings as in Fig. 9.

reverses and is not well calibrated. Below the imposed lower bound of  $\alpha_s$  the resulting CCF becomes insensitive to the value of  $\alpha_s$ .

Note that there are 113 objects in common between the 2MASS galaxy sample and *Swift*/*INTEGRAL* AGN sample. In principle, this affects the satellite-satellite pair counts in the one-halo term calculation of the CCF in the HOD modelling (see paper II). However, since only 0.3% of the 2MASS galaxies are common, the effect of these objects in the pair count is negligible.

## 4 RESULTS

Fig. 9 shows our measured 2MASS galaxy ACF with the best-fitting HOD model and fit residuals. The best-fit HOD model (with  $\chi^2/\text{d.o.f.} = 0.99$ ) corresponds to  $\log M_{\min} = \log M_0 = 12.50^{+0.23}_{-0.01}$ ,  $\sigma_{\log M} = 0.42^{+0.31}_{-0.01}$ ,  $\log (M'_1/M_0) = 1.10^{+0.01}_{-0.27}$  and  $\alpha_s = 1.13^{+0.05}_{-0.07}$ . The quoted uncertainty intervals correspond to  $\Delta\chi^2 < 7.78$  (90% confidence region in four free parameters). The large-scale bias parameter of our 2MASS galaxy sample is  $b = 1.25^{+0.02}_{-0.03}$ .

The magnitude limit of our 2MASS galaxy sample is  $M_{K_s} = -24.4$ . We use the stellar population model of Worthey et al. (1994)<sup>4</sup> to determine a rough estimate on the corresponding SDSS *r*-band magnitude. We use an old stellar population model (10 Gyr, solar metallicity), which leads to  $r - K = 3$  and predicts that our 2MASS galaxies are brighter than  $M_r \sim -21.4$ . Indeed, our HOD results for 2MASS galaxies agree well with the HOD results presented in Zehavi et al. (2011) (see their table 3) for  $M_r^{\max} = -21$ . Recall that we apply an upper cut on

$M_{K_s} = -25.9$ , while the luminosity-threshold samples in Zehavi et al. (2011) have only a lower  $M_r$  limit. Thus, our 2MASS sample excludes the brightest and most massive galaxies. This naturally drives the HOD results to lower values in  $\log M_{\min}$  than the  $M_r^{\max} = -21.5$  sample in Zehavi et al. (2011).

The best-fitting HOD model to the CCF between 2MASS galaxies and the full AGN sample is shown in Fig. 10. From this fit we derive the large-scale bias parameter listed in Table 1 and confidence contours for both the minimum DMH mass needed to harbour an AGN and the satellite slope  $\alpha_s$  (see Fig. 12 panel a). The measured CCF and the best-fitting HOD model for the subsamples defined with respect to  $L_X$ , AGN type classification and X-ray photon index  $\Gamma$  are presented in Fig. 11. The HOD model parameter confidence contours are shown in Fig. 12. As discussed below, for the subsamples defined by  $L_X$  and AGN type classification, these two-dimensional contours have the advantage of showing a clear difference between the subsamples which is not detected when collapsing all information into a one-dimensional parameter such as the large-scale bias.

For each sample we list in Table 1 the number of objects, the mean effective redshift of  $N_{\text{CCF}}(z)$ , the median 14–195 keV luminosity, the median photon index  $\Gamma$  and the HOD-derived large-scale bias parameter. Since we measure the CCF, the resulting effective redshift distribution for the clustering signal is determined by both the redshift distribution of the tracer set and the AGN sample:  $N_{\text{CCF}}(z) = N_{\text{tracer}}(z) * N_{\text{AGN}}(z)$ .

From the HOD model, the bias parameter can be calculated using

$$b_{\text{HOD}} = \frac{\int b(M_h) \langle N_A \rangle (M_h) \phi(M_h) dM_h}{\int \langle N_A \rangle (M_h) \phi(M_h) dM_h}, \quad (8)$$

where  $\phi(M_h)$  is the halo mass function. Defining  $b_{\text{OBS,HOD}}$  as the bias parameter obtained from the best-fitting HOD model to the observed CCF using equation 8, we then define the typical DMH mass  $M_h^{\text{typ}}$  by  $b(M_h^{\text{typ}}) = b_{\text{OBS,HOD}}$ . This conversion is performed using the same halo mass function, linear power-spectrum and  $b(M)$  relation as those used in the HOD calculation. For all AGN samples, the HOD calculations are based on  $z = 0.02$ . The values given for  $M_h^{\text{typ}}$  increase by only 0.01 at  $z = 0.03$ .

Note that the conversion between the measured  $b_{\text{OBS,HOD}}$  to  $M_h^{\text{typ}}$  in our previous papers was based on the analytical approximation of the  $\nu - M_h$  relation by van den Bosch (2002), where  $\nu$  is the ratio of the spherical overdensity required for collapse to the root mean square density fluctuation on the scale  $r$  of the initial size of the object  $M_h$ . However, in this work this conversion is based on the linear power spectrum generated by the software *camb* (see above), to be consistent with the HOD model calculation itself. This change in procedure results in approximately 0.2 dex higher  $M_h^{\text{typ}}$  for the same bias value; for example, the full AGN sample would have  $\log (M_h^{\text{typ}} [h^{-1} M_\odot]) = 13.02$ . This is important to consider when comparing  $M_h^{\text{typ}}$  from our various papers.

We also calculate the mean DMH mass from the HOD model, using

$$\langle M_h \rangle = \frac{\int M_h \langle N_A \rangle (M_h) \phi(M_h) dM_h}{\int \langle N_A \rangle (M_h) \phi(M_h) dM_h}. \quad (9)$$

<sup>4</sup> [http://astro.wsu.edu/dial/dial\\_a\\_model.html](http://astro.wsu.edu/dial/dial_a_model.html)

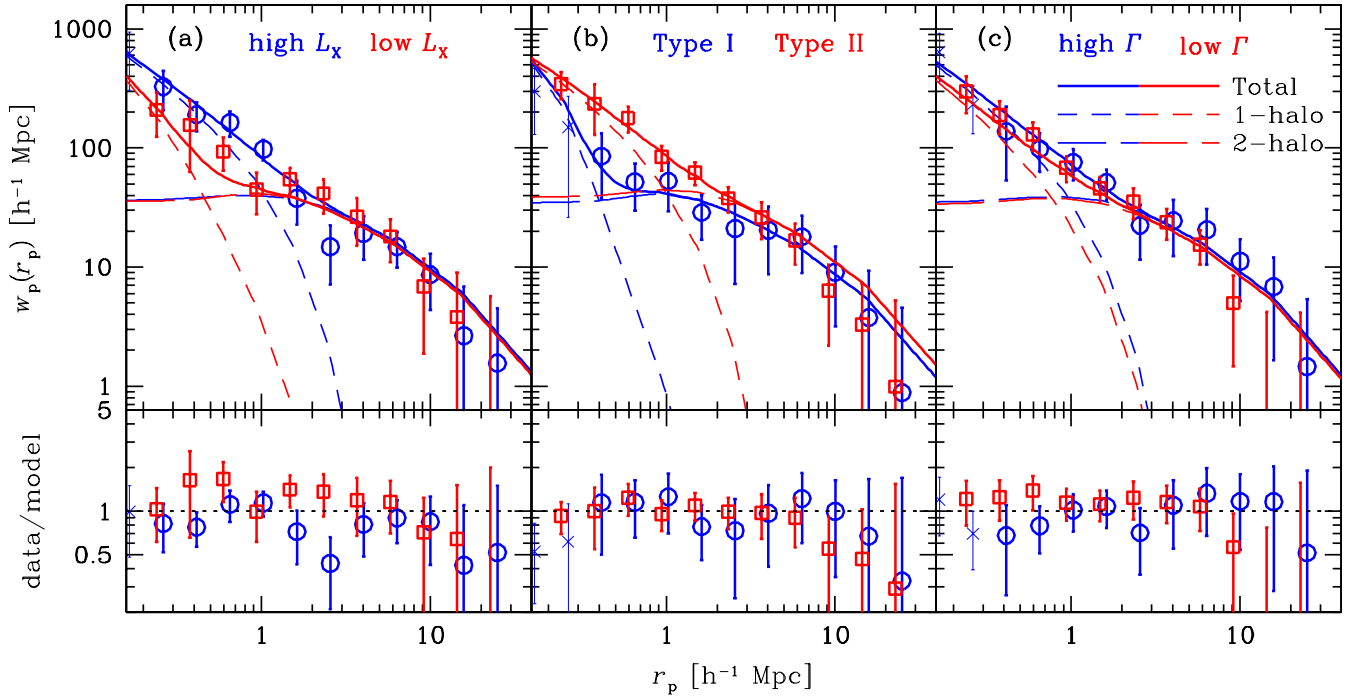


**Figure 11.** Similar to Fig. 10, here showing a comparison of the best-fitting HOD models and fit residuals for the  $L_X$  samples (panel a), type I versus type II samples (panel b) and X-ray photon index  $\Gamma$  (panel c). Data points shown as crosses are excluded in the  $\chi^2$  fitting process as they represent bins with less than 16 pairs.

**Table 1.** Properties of the AGN samples and their derived HOD modelling quantities.

AGN sample name	Number of objects	Mean $z_{\text{eff}}$	Median log $L_{14-195 \text{ keV}}^\dagger$	Median $\Gamma$	$b(z)$ (HOD)	$\log M_h^{\text{typ}} (h^{-1} M_\odot)$	$\log \langle M_h \rangle (h^{-1} M_\odot)$
Full AGN sample	274	0.028	43.42	1.92	$1.04^{+0.10}_{-0.11}$	$12.84^{+0.22}_{-0.30}$	$13.44^{+0.05}_{-0.07}$
Low- $L_X$ AGN sample	139	0.023	43.17	1.92	$0.98^{+0.05}_{-0.07}$	$12.70^{+0.12}_{-0.22}$	$12.94^{+0.17}_{-0.26}$
High- $L_X$ AGN sample <sup>‡</sup>	135	0.030	43.69	1.90	$1.04^{+0.05}_{-0.04}$	$12.84^{+0.12}_{-0.10}$	$13.55^{+0.06}_{-0.05}$
Type I AGN sample	113	0.025	43.45	2.01	$0.96^{+0.05}_{-0.12}$	$12.64^{+0.14}_{-0.44}$	$12.75^{+0.18}_{-0.27}$
Type II AGN sample <sup>‡</sup>	157	0.027	43.36	1.85	$1.17^{+0.08}_{-0.13}$	$13.10^{+0.12}_{-0.26}$	$13.56^{+0.05}_{-0.09}$
Low- $\Gamma$ AGN sample	137	0.028	43.40	1.76	$0.90^{+0.15}_{-0.05}$	$12.45^{+0.41}_{-0.19}$	$13.27^{+0.07}_{-0.10}$
High- $\Gamma$ AGN sample	124	0.029	43.42	2.07	$0.98^{+0.15}_{-0.05}$	$12.70^{+0.34}_{-0.16}$	$13.45^{+0.07}_{-0.08}$

<sup>†</sup> $L_{14-195 \text{ keV}}$  is given in units of  $\text{erg s}^{-1}$ .

<sup>‡</sup>For the high- $L_X$  AGN sample the best fit is pegged at the lower bound of the parameter grid,  $\log(M_{\text{min}} [h^{-1} M_\odot]) = 9.8$ . The type I AGN sample is pegged at  $\alpha_s = -0.6$ .

The mean halo mass is similar to  $M_h^{\text{typ}}$  in that they are both representative halo masses of the sample. Comparing equations 8 and 9, one can see that the mean mass gives more weight to higher DMH masses, as, for example,  $b(M_h)$  increases only from  $\sim 0.8$  to  $\sim 1.1$  as  $\log \langle M_h [h^{-1} M_\odot] \rangle$  increases from 12.0 to 13.0. We note that  $M_h^{\text{typ}}$  is almost solely determined by the two-halo term and is thus insensitive to the CCF in the one-halo regime, while both the one-halo and two-halo terms affect  $\langle M_h \rangle$ .

For the full AGN sample, we find a large-scale bias parameter of  $1.04^{+0.10}_{-0.11}$ . Comparing only the bias parameters, we find that none of the AGN subsamples defined by

$L_X$ , type or  $\Gamma$  show statistically significant differences in the large-scale bias. All differences are  $< 1.5\sigma$  when considering the combined uncertainties. However, comparing the subsamples defined by  $L_X$  and type, there are significant differences in  $\log \langle M_h \rangle$ . Type I and type II AGN differ in their mean halo mass  $\langle M_h \rangle$  at the  $4.0\sigma$  level in that type II AGN have a larger  $\langle M_h \rangle$  than type I AGN. Low- $L_X$  AGN also have a lower  $\langle M_h \rangle$  than high- $L_X$  AGN with a  $3.4\sigma$  difference.

Figs 11(a) and (b) and 12(a) and (b) show that these significant differences in the clustering properties are caused by differences in the one-halo term, i.e., the CCF contributed by pairs within the same DMH. Low- and high- $L_X$  AGN popu-

late DMHs differently, in that higher *minimum* DMH masses are required to host low- $L_X$  AGN compared to their high- $L_X$  counterparts. In addition, with increasing DMH mass the fraction of high- to low- $L_X$  AGN in satellite galaxies increases, as seen in the different values of  $\alpha_s$ . Type I and type II AGN require similar  $M_{\min}$  to host such AGN (see Fig. 12). However, they occupy DMHs differently, in that with increasing DMH mass the number of type I AGN in satellite galaxies decreases while the number of type II AGN rises proportionally with increasing DMH mass.

#### 4.1 Robustness of Clustering Measurements

We have paid considerable attention in this paper to creating robust clustering measurements, including careful sample selection and testing our results for possible systematic errors. First, as discussed above, we chose a redshift and absolute luminosity range for the 2MASS galaxies such that splitting the full sample into lower and higher redshift bins results in only marginal differences in the clustering signal. For the lower redshift 2MASS sample we use a redshift range of  $0.007 < z \leq 0.025$  and for the higher redshift sample we use  $0.025 < z < 0.037$ . This results in 2681 and 6470 galaxies in the lower and higher redshift samples, respectively. Considering the available comoving volumes within these redshift intervals, the two projected correlation functions have very similar S/Ns, and all data points for the lower and higher redshift 2MASS correlation functions agree well within their  $1\sigma$  uncertainties.

Secondly, we tested removing all *INTEGRAL* AGN from the full AGN sample and subsamples. The resulting bias values agree with those listed in Table 1 within their combined  $1\sigma$  uncertainties. For example, the type I and type II AGN subsample using only the 70-month *SWIFT*/BAT catalogue have bias values of  $b_{\text{typeI}} = 0.98^{+0.05}_{-0.11}$  and  $b_{\text{typeII}} = 1.19^{+0.11}_{-0.07}$ . The corresponding mean halo masses for type I and II AGN are  $\langle M_{h,\text{typeI}} \rangle = 12.81^{+0.13}_{-0.27}$  and  $\langle M_{h,\text{typeII}} \rangle = 13.60^{+0.08}_{-0.06}$ . The similarity of these values to the ones listed in Table 1 indicates that our results are robust to the inclusion of *INTEGRAL* AGN.

Thirdly, to further check how sensitive the best fit and corresponding contours are to moderate changes in the sample selection, we randomly removed 15% of objects in each of the type I and type II subsamples. We then recomputed the CCF and reran the HOD modelling and find bias values of  $0.93^{+0.08}_{-0.09}$  for type I AGN and  $1.06^{+0.14}_{-0.06}$  for type II AGN (which differ from each other at the  $1\sigma$  level). The resulting mean halo masses of  $\langle M_{h,\text{typeI}} \rangle = 12.72^{+0.22}_{-0.30}$  and  $\langle M_{h,\text{typeII}} \rangle = 13.50^{+0.09}_{-0.03}$  differ at a  $3.5\sigma$  level and the HOD-derived contours look almost identical to the ones shown in Fig. 12 (panel b). We also reran the HOD modelling using uncorrelated  $\chi^2$  fitting and confirm all of our results within  $1\sigma$  of the bias values and mean halo masses listed in Table 1 and recover similar confidence contours.

Fourthly, we tested excluding in the HOD fitting the scales which could be affected by the halo-halo collision. Again, the resulting bias values and confidence contours agree well within their  $1\sigma$  uncertainties.

Fifthly, we check whether or not the difference in redshift and X-ray luminosity between type I and II AGN (see Figs 3 and 5) causes the discrepancy in the clustering properties. For this test, we create matched redshift distributions

for type I and II AGN. This matching of the subsamples is a commonly used method in clustering measurements to remove possible observation biases or correlations between parameters (e.g., Coil et al. 2009; Krumpe et al. 2015). In the case of redshift matching, we trim the type II AGN redshift range to that of the type I AGN. Then, if there are more type II AGN in a given redshift bin than type I AGN, we randomly select the same number of type II AGN as type I AGN. If there are fewer type II AGN than type I AGN, we upweight type I AGN to have the same number as type II AGN. This ensures that the type I and II AGN have the same redshift distribution in our clustering measurements. We also test randomly selecting a subset of AGN of a given type so as to match the number of AGN of the other type, in a given redshift bin. The identical procedures are applied for matching the luminosity distributions.

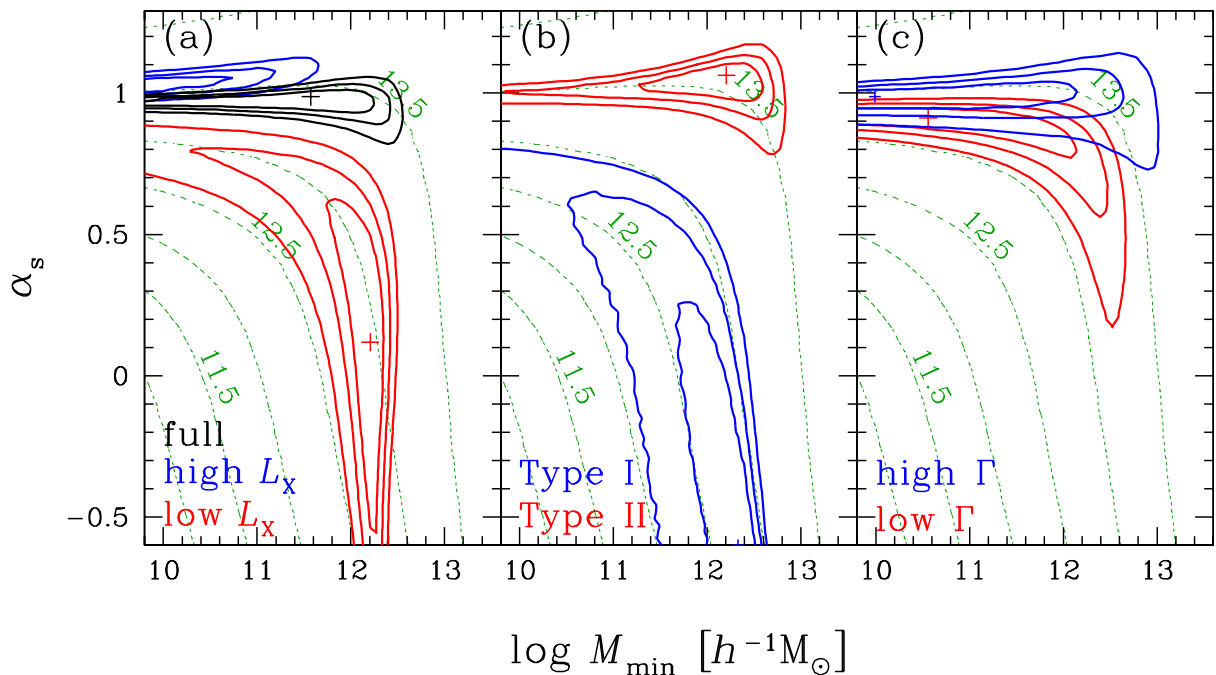
In the cases of matched redshift distributions for type I and type II AGN, we do not detect any significant deviation from the full type I and type II samples in Table 1. All realizations of type I samples (based on matched distributions) have  $\log \langle M_h \rangle = 12.70 - 12.81 h^{-1} M_\odot$  with maximal uncertainties of  $^{+0.27}_{-0.55}$ . The corresponding type II samples result in  $\log \langle M_h \rangle = 13.45 - 13.56 h^{-1} M_\odot$  with maximal uncertainties of  $^{+0.11}_{-0.13}$ . In particular, the constraints on  $\alpha_s$  for type I and type II are very similar to those shown in Fig. 12.

Fig. 5 shows that at extremely low and high X-ray luminosities there is little to no overlap between type I and type II AGN. Thus, we restrict the X-ray luminosity range used for matching to  $42.6 \leq \log (L_{14-195 \text{ keV}} / [\text{erg s}^{-1}]) \leq 44.6$ . This restriction and the matching procedure itself leads to a significant loss in the number of sources in the type I and II samples. Consequently, the error bars on our individual measurements increase substantially. For the same reason, the confidence contours as shown in Fig. 12 (panel b) increase but the result that type I and type II AGN have significantly different clustering remains.

Sixthly, we also test whether the difference in the HOD parameters between the low- and high- $L_X$  samples is due to differences in their redshift distributions. The matching procedure described above is not useful here, as the redshift distributions between the low and high  $L_X$  samples differ substantially, and more than half of the AGN would have to be removed to match these distributions. Thus, we create three redshift subsamples as follows: (i)  $0.007 \leq z < 0.017$ , (ii)  $0.017 \leq z < 0.027$ , and (iii)  $0.027 \leq z \leq 0.037$ . In each redshift range, we determine the median  $L_X$  and divide the sample into low- and high- $L_X$  samples. Finally, we add all low- and high- $L_X$  subsamples of the three individual redshift ranges. This approach produces very similar redshift distributions between the final low- and high- $L_X$  samples.

For these samples, we find  $\log \langle M_{h,\text{low}L_X} \rangle = 12.95^{+0.21}_{-0.47} h^{-1} M_\odot$  and  $\log \langle M_{h,\text{high}L_X} \rangle = 13.61^{+0.04}_{-0.07} h^{-1} M_\odot$ . This is in excellent agreement with the values given in Table 4. The resulting HOD contours are very similar to the ones shown in Fig. 12 (panel a). Only the  $\alpha_s$  best-fitting value of the low- $L_X$  sample shifts to  $\alpha_s \sim 0.68$ .

In summary, we conclude that our results are not significantly impacted by systematic effects and are robust to moderate changes in our methodology and sample selection. In particular, the significant clustering difference in the mean halo masses of type I and type II AGN remains when modifying the sample selection.



**Figure 12.** Confidence contours of the HOD-derived parameters  $\alpha_s$  (satellite slope) and  $\log M_{\min}$  (minimum halo mass to host an AGN) for the (a) full (black), low and high  $L_X$ , (b) type I and type II classified and (c) X-ray photon index divided samples. The colour coding of the subsamples is identical to the ones used in Fig. 11. The confidence intervals correspond to  $\Delta\chi^2 = 1.0, 2.3$  and  $4.6$  levels. The green dashed lines show the mean DMH mass in  $\log\langle M_h \rangle [h^{-1} M_\odot]$  derived from the model parameters as labelled.

## 5 DISCUSSION

For the full hard X-ray-selected AGN sample we find slightly lower bias values than those reported in Cappelluti et al. (2010). However, the results differ by only  $1.4\sigma$ , and this small difference is not surprising as different methods are used in each study to compute the bias. Cappelluti et al. (2010) performed power-law fits to the projected ACF, while we use the HOD modelling approach. For this comparison, we use bias values rather than estimated  $M_h^{\text{typ}}$ , as different methods are used in the literature to compute  $M_h^{\text{typ}}$ , which can lead to severe systematics and misinterpretations (see also the discussion on this issue in paper IV, end of Section 5).

Although these differences in the methodology used to convert bias into  $M_h^{\text{typ}}$  exist in the literature, here we can confirm the overall picture of AGN clustering that has emerged, in that even in the very local Universe AGN prefer DMH masses of  $M_h^{\text{typ}} \sim 10^{13} h^{-1} M_\odot$ , as they do at higher redshifts. In Fig. 13 we show local and low-redshift measurements of X-ray-selected AGN that are all based on the cross-correlation technique. The finding that AGN inhabit group-mass haloes holds at least up to a redshift of  $z \sim 3$  (see, e.g., fig. 5 of Allevato et al. 2016). When comparing the clustering measurements of AGN to those of blue and red galaxies (e.g., Madgwick et al. 2003, Zehavi et al. 2005, Hickox et al. 2009), local AGN seem to be hosted by a mix of blue and red galaxies. This finding is consistent with that of Li et al. (2006), who find that narrow-line AGN host galaxies and inactive control galaxies populate DMH of similar mass.

### 5.1 Clustering dependence on X-ray luminosity

Using the measured ACF of 199 *SWIFT*/BAT AGN, Cappelluti et al. (2010) find an X-ray luminosity dependence on the clustering strength at the  $1.6\sigma$  level, using derived large-scale bias values. Here our bias values for the low- and high- $L_X$  subsamples are also not statistically significantly different, with a difference of only  $0.9\sigma$  (see Table 1).

At other redshifts, we detected a weak X-ray luminosity dependence (see Fig. 13; papers III and IV) based on the derived bias values. In Krumpe et al. (2015) (paper IV), we showed at  $z = 0.16 - 0.36$  that the physical origin of high- $L_X$  AGN being more clustered than low- $L_X$  AGN is a difference in black hole mass, i.e., larger supermassive black holes reside in larger DMH masses. It is therefore not that an overdensity of galaxies leads to a higher accretion rate on to the supermassive black hole(s).

The low number of objects in the low- and high- $L_X$  subsamples in this paper might hamper our ability to detect any luminosity-dependence in the clustering strength in the local Universe. We will need to rely on much larger AGN samples available in the future to test this. For comparison, 1552 RASS AGN and  $\sim 46\,000$  luminous red galaxies were used at  $z = 0.16 - 0.36$  to detect the weak X-ray luminosity dependence that was observed.

However, Fig. 11 (a) shows differences between the  $L_X$  subsamples in the one-halo term regime, and the  $\log\langle M_h \rangle$  value of the high- $L_X$  sample is larger than that of the low- $L_X$  sample by  $\sim 3.4\sigma$ . The confidence contours shown in Fig. 12 for these two subsamples occupy completely separate regions of this space. In particular,  $\alpha_s \sim 1$  for the high- $L_X$  subsample, which is higher than that for the low- $L_X$  sample, indicating a greater abundance of high- $L_X$  AGN in satellite



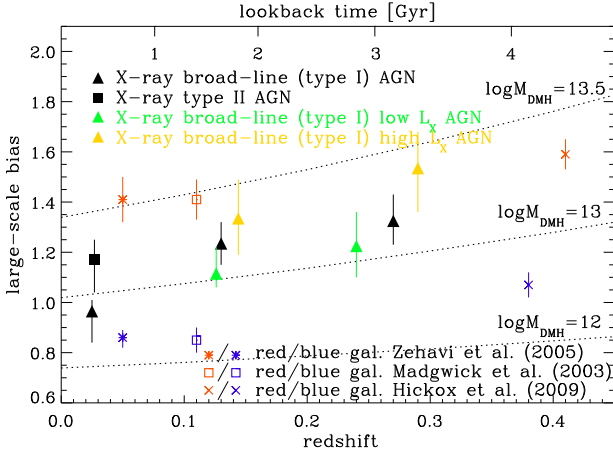


**Figure 13.** Large-scale bias as a function of redshift for various X-ray-selected AGN samples, compared to red and blue galaxies (red and blue symbols). Black filled triangles show X-ray-selected type I AGN from this study and Krumpe et al. (2012, 2015) at higher redshift. Luminosity-dependent subsamples of X-ray-selected type I AGN are shown as green (low- $L_X$ ) and yellow (high- $L_X$ ) filled triangles. The black filled box shows type II AGN from this study. The biases for all AGN samples are computed by HOD modelling, while the galaxy clustering bias is based on power-law fits to the observed correlation function. The dotted lines show the expected  $b(z)$  of DMH masses  $M_h^{\text{typ}}$  based on Sheth et al. (2001) and the improved fit for this equation given by Tinker et al. (2005). The masses are given in  $\log M_h^{\text{typ}}$  in units of  $h^{-1} M_\odot$ .

galaxies in the most massive haloes. This contributes to the increased clustering seen in the CCF of the high- $L_X$  sample at  $r_p \sim 1 h^{-1} \text{Mpc}$ . Therefore we do find significantly different clustering properties for the high- and low- $L_X$  samples, even if this is not reflected in the large-scale bias term alone.

We emphasize that our other papers (papers I–IV) are all based on soft X-ray selected, optically confirmed, broad emission-line AGN. The AGN sample presented here is hard X-ray selected and a mix of  $\sim 42\%$  type I (broad line) and  $\sim 58\%$  type II (narrow-line) AGN. Unfortunately, the low number of objects in each type does not allow us to further divide these samples with respect to X-ray luminosity.

## 5.2 Clustering dependence on black hole mass

Using the black hole mass estimates of Koss et al. (2017), we test for a clustering dependence on black hole mass for local AGN. No significant difference is found between the bias values or  $\log \langle M_h \rangle$  of the low and high  $M_{\text{BH}}$  subsamples ( $b_{\text{low}M_{\text{BH}}} = 1.03^{+0.12}_{-0.12}$ ,  $b_{\text{high}M_{\text{BH}}} = 0.98^{+0.04}_{-0.02}$ ,  $\log \langle M_{h,\text{low}M_{\text{BH}}} \rangle = 13.15^{+0.17}_{-0.38}$  and  $\log \langle M_{h,\text{high}M_{\text{BH}}} \rangle = 13.45^{+0.05}_{-0.02}$ ).

We suffer from three challenges in possibly detecting a dependence of clustering on  $M_{\text{BH}}$ . First, we suffer from a further decrease in sample size as only  $\sim 60\%$  of local *SWIFT*/BAT AGN have black hole mass estimates thus far. Secondly, paper IV shows that the strength of the observed  $M_{\text{BH}}$  dependence at higher redshift is weak and of similar amplitude as the weak  $L_X$  dependence. As discussed above, we do not detect a statistically significant  $L_X$  dependence on

the clustering for local AGN using the large-scale bias values, though we do detect differences in the one-halo term.

Thirdly, there is a substantial difference in the mean black hole mass estimated at a given  $L_X$  for the two methods used in Koss et al. (2017) (see Fig. 8). The linear fits of the black hole masses derived from the different methods each show a correlation between  $L_X$  and  $M_{\text{BH}}$ , offset by about an order of magnitude, depending on which method is used. Given the large possible systematic difference in the masses derived using these two methods, we attempted to measure the clustering dependence on  $M_{\text{BH}}$  using masses derived just with the stellar velocity dispersion method, which has more estimated black hole masses. However, this results in too few objects to derive a constrained CCF measurement.

We conclude that the non-existence of a clustering dependence with black hole mass in the local Universe cannot be ruled out with the present limited data. This will be an interesting test for future studies of local AGN with larger samples with black hole mass estimates.

## 5.3 Clustering differences for type I and II AGN

In contrast to Cappelluti et al. (2010), we do not find that type I AGN have a higher bias value than type II AGN. In detail, the bias values for type I AGN differ significantly between these two studies (by  $\sim 7\sigma$ ), while the values for type II AGN agree well within their uncertainties. In our directly measured CCFs between the type I and type II AGN and the 2MASS galaxy sample, the difference is clearly visible at small and intermediate scales (Fig. 11). The HOD fits provide further insights into the different clustering properties of type I and type II AGN. The confidence contours of  $\log M_{\text{min}}$  and  $\alpha$  shown in Fig. 12 demonstrate a clear difference in the clustering properties of type I versus type II AGN, and we detect a difference in  $\log \langle M_h \rangle$  at the  $4\sigma$  level, similar to the difference seen between the low and high  $L_X$  samples.

Type I AGN have a much shallower satellite slope  $\alpha_s$  than type II AGN. The slope found here for type I AGN is consistent with that of type I AGN at higher redshifts (see paper II and e.g. Allevato et al. 2012). Thus, it appears that with increasing DMH mass the duty cycle of type I AGN in satellite galaxies decreases. This could possibly be explained by AGN triggering of major and minor mergers of sub-haloes inside group mass host DMHs, as the merging cross-section decreases in the high relative velocity encounters that are more common as the DMH mass increases (Altamirano-Dévorra et al. 2016). At least for local type II AGN this appears not to be the dominant triggering mechanism, as they have an HOD satellite slope that is similar to that of galaxies. Thus, the type II AGN duty cycle in satellite galaxies is close to constant with increasing DMH mass. Therefore, type II AGN should have a higher duty cycle in more massive DMHs than type I AGN. This suggests that the dominant triggering mechanism of type II AGN in groups and clusters is not mergers but more likely disturbances due to close encounters and/or secular processes.

The type I and type II AGN samples have very similar median X-ray luminosities (see Table 1) as well as similar X-ray luminosity distributions (Fig. 5). We tested matching their redshift and X-ray luminosity distributions and find similar results (see Section 4.1). Thus, the different clus-

tering properties of type II AGN compared to type I AGN cannot be explained by the observed X-ray luminosity dependence of the clustering signal.

According to a simple orientation-based AGN unification scheme, in which type I and type II AGN should have similar distributions of properties such as redshift, luminosity and black hole mass, no statistical difference is expected in their clustering behaviour. Thus, our results contradict a simple AGN unification model, at least for the local Universe.

Other studies also find evidence that type I and type II AGN might reside in different environments. Villarroel & Korn (2014) conduct number counts around type I (broad-line) and type II (narrow-line) AGN at  $0.03 < z < 0.2$ . Their results are also inconsistent with a simple orientation-based AGN unification scheme. They find, for example, that the average colour of the neighbours is redder around type I AGN than around type II and that the fraction of AGN in spiral host galaxies depends on AGN type. Other studies use different samples but similar methods and find contradictory results. For example, Jiang et al. (2016) find that type II AGN have significantly more satellites than type I AGN do, while Gordon et al. (2017) cannot confirm such a difference.

As shown in Fig. 6, separating AGN by type is similar to separating AGN by the amount of absorbing column density  $N_H$ . This suggests that future studies may be able to detect a weak clustering dependence on  $N_H$  in the local Universe, as obscured AGN should show similar clustering properties as type II AGN.

#### 5.4 Clustering Dependence on Photon Index

Trakhtenbrot et al. (2017) analysed 228 BAT AGN in the redshift range of  $0.01 < z < 0.5$  for which black hole mass estimates are available. They found a weak correlation between photon index and accretion rate of the black holes in that, on average, higher photon index corresponds to higher accretion ratio relative to Eddington. Thus, measuring the clustering dependence on the photon index might reflect the dependence on accretion rate as well. We note that Trakhtenbrot et al. (2017) determine their photon index in the 2–10 keV band, unlike what is used in this study.

Here we do not find a significant clustering dependence on photon index determined in the 14–195 or 20–200 keV bands. Thus it would appear that there is likely no strong clustering dependence on accretion ratio relative to Eddington. In paper IV, we also tested for a clustering dependence on accretion ratio using a soft X-ray-selected broad emission-line AGN sample and did not find a correlation either. Aird et al. (2012) show that the accretion rate relative to Eddington does not strongly depend on stellar mass of the host galaxy. Thus, it might not be surprising that the clustering dependence on accretion ratio, if it exists at all, should be very weak.

## 6 CONCLUSIONS

We explore the clustering properties of hard X-ray-selected AGN in the local Universe. This study is the most precise clustering measurement made to date for AGN at very low

redshift; the median redshift of  $z = 0.024$  corresponds to a look-back time of only 330 million years. Selecting AGN using hard X-rays (14–195 and 20–200 keV bands) allows a measurement of AGN clustering that is unbiased with respect to absorption. We achieve the high precision by using a cross-correlation approach, in that we compute the two-point CCF between the AGN sample and a much larger sample of 2MASS galaxies which acts as a tracer set of the large-scale matter distribution in the local Universe. We then perform HOD modelling to the CCF to derive the large-scale bias parameter and determine the distribution of AGN within DMHs. As a by-product of our cross-correlation technique, we also report here for the first time an HOD model of 2MASS-selected galaxies, for  $0.007 \leq z \leq 0.037$  and  $-24.4 \leq M_{K_s} \leq -25.9$  (see Section 4).

We analyse the clustering properties not only for the full AGN sample but also for subsamples defined by X-ray luminosity, type I versus type II classification, photon index of the X-ray spectrum and black hole mass. The full AGN sample ( $0.007 < z < 0.037$ ) has a bias parameter of  $b = 1.04^{+0.10}_{-0.11}$ , which corresponds to a typical host DMH mass of  $M_h^{\text{typ}} = 12.84^{+0.22}_{-0.30} h^{-1} M_\odot$ .

Comparing the large-scale bias values, we do not find statistically significant differences in the subsamples as a function of X-ray luminosity, AGN type classification, photon index and black hole mass. In Krumpe et al. (2015) we showed that at  $z \sim 0.3$  only a weak clustering dependence as a function of X-ray luminosity and black hole mass exists. The moderate sample sizes used here (when splitting the full AGN sample with respect to the different AGN parameters) may hamper our ability to detect such a weak clustering dependence in the local Universe. However, the joint two-dimensional space that is fit by our AGN HOD model (which constrains the minimum DHM mass required to host an AGN and the satellite slope), as well as the mean halo mass, do show significant clustering differences for AGN as a function of X-ray luminosity. We find that high X-ray luminosity AGN have a larger mean halo mass than their low-luminosity counterparts at the  $3.4\sigma$  level.

We also find significant differences in the clustering properties of type I and type II AGN. While similar minimum halo masses are required to host type I and type II AGN, type II AGN have a higher *mean* halo mass than type I AGN, at the  $4.0\sigma$  level. As found previously at other redshifts (Miyaji et al. 2011; Allevato et al. 2012), our HOD model for local type I AGN indicates that above DMH masses of  $M_h \sim 10^{12} h^{-1} M_\odot$  the duty cycle of AGN in satellite galaxies decreases with increasing halo mass, in that the slope of the HOD is shallower for AGN than for galaxies. In contrast, local type II AGN have an HOD that is very similar to that of galaxies. The average number of type II AGN in satellite galaxies increases approximately proportionally to DMH mass, as is observed for galaxies. Thus, the ratio of type I to II AGN should decrease with DMH mass. These differences in the clustering properties of type I and type II AGN are at odds with a simple orientation-based AGN unification scheme.

This study demonstrates that testing the clustering properties of AGN with respect to AGN parameters such as redshift, luminosity and classification not only enhances our understanding of how AGN populate DMHs through cosmic time, but that such measurements can constrain AGN mod-

els such as the unification model which, at first glance, may seem to have no connection to large-scale structure. Extending this approach with much larger samples will allow us to significantly constrain physical models of AGN triggering and evolution.

## ACKNOWLEDGEMENTS

We would like to thank Lutz Wisotzki for helpful discussions and supporting this project. MK acknowledges support by DFG grant KR 3338/3-1. TM and HA thank for financial support by CONACyT Grant Científica Básica #252531, UNAM-DGAPA Grants PAPIIT IN104113 and IN104216. This publication makes use of data products from the 2MASS, which is a joint project of the University of Massachusetts and the Infrared Processing and Analysis Center/California Institute of Technology, funded by the National Aeronautics and Space Administration and the National Science Foundation. This work is based on data taken by *SWIFT*, a MIDEX mission led by NASA with participation of Italy and the UK. We thank Angela Malizia for providing the *INTEGRAL*/IBIS catalogues. This study is based on *INTEGRAL* data. This research has made use of data and/or software provided by the High Energy Astrophysics Science Archive Research Center (HEASARC), which is a service of the Astrophysics Science Division at NASA/GSFC and the High Energy Astrophysics Division of the Smithsonian Astrophysical Observatory. This research has made use of data and/or software provided by the High Energy Astrophysics Science Archive Research Center (HEASARC), which is a service of the Astrophysics Science Division at NASA/GSFC and the High Energy Astrophysics Division of the Smithsonian Astrophysical Observatory. We also thank the referee for a useful report.

## REFERENCES

- Aird, J., Coil, A.L., Georgakakis, A., et al. 2015, MNRAS, 451, 1892
- Aird, J., Coil, A.L., Moustakas, J., et al. 2012, ApJ, 746, 90
- Altamirano-Dévora, L., Miyaji, T., Aceves, H., et al. 2016, Rev. Mex. Astron. Astrofis., 52, 11
- Ajello, M., Costamante, L., Sambruna, R.M., et al. 2009, ApJ, 699, 603
- Allevato, V., Civano, F., Finoguenov, A., et al. 2016, ApJ, 832, 70
- Allevato, V., Finoguenov, A., Hasinger, G., et al. 2012, ApJ, 758, 47
- Allevato, V., Finoguenov, A., Cappelluti, N., et al. 2011, ApJ, 736, 99
- Baumgartner, W.H., Tueller, J., Markwardt, C.B., et al. 2013, ApJS, 207, 19
- Bird, A.J., Bazzano, A., Malizia, A., et al. 2016, ApJS, 223, 15
- Cappelluti, N., Ajello, M., Burlon, D., et al. 2010, ApJ, 716L, 209
- Coil, A.L., Georgakakis, A., Newmann, J.A., et al. 2009, ApJ, 701, 1484
- Davis, M. & Peebles, P.J.E. 1983, ApJ, 267, 465
- Gehrels, N., Chincarini, G., Giommi, P., et al. 2004, ApJ, 611, 1005
- Gordon, Y.A., Owers, M.S., Pimblet, K.A., et al. 2017, MNRAS, 465, 2671
- Hickox, R.C., Jones, C., Forman, W.R., et al. 2009, ApJ, 696, 891
- Huchra, J.P., Macri, L.M., Masters, K.L., et al. 2012, ApJS, 199, 26
- Jarrett, T. 2004, PASA, 21, 396
- Jiang, N., Wang, H., Mo, H., et al. 2016, ApJ, 832, 111
- Kauffmann, G., Heckman, T.M., Tremonti, C., et al. 2003, MNRAS, 346, 1055
- Komiya, Y., Shirasaki, Y., Ohishi, M., & Mizumoto, Y. 2013, ApJ, 775, 43
- Koss, M., Trakhtenbrot, B., Ricci, C., et al. 2017, ApJ, 850, 74
- Koutoulidis, L., Plionis, M., Georgantopoulos, I., & Fanidakis, N. 2013, MNRAS, 428, 1328
- Krumpe, M., Miyaji, T., & Coil, A.L. 2010 ApJ, 713, 558 (paper I)
- Krumpe, M., Miyaji, T., & Coil, A.L., & Aceves, H. 2012 ApJ, 746, 1 (paper III)
- Krumpe, M., Miyaji, T., & Coil, A.L. 2014 Acta Polytechnica CTU, 71
- Krumpe, M., Miyaji, T., Husemann, B., et al. 2015 ApJ, 815, 21 (paper IV)
- Landy, S.D. & Szalay, A.S. 1993, ApJ, 412, 64
- Larson, D., Dunkley, J., Hinshaw, G., et al. 2011, ApJS, 192, 16
- Li, C., Kauffmann, G., Wang, L., et al. 2006, MNRAS, 373, 457
- Madgwick, D.S., Hawkins, E., Lahav, O., et al. 2003, MNRAS, 344, 847
- Malizia, A., Bassani, L., Bazzano, A., et al. 2012, MNRAS, 426, 1750
- Malizia, A., Landi, R., Molina, M., et al. 2016, MNRAS, 460, 19
- Mandelbaum, R., Li, C., Kauffmann, G., et al. 2009, MNRAS, 393, 377
- Miyaji, T., Krumpe, M., Coil, A.L., & Aceves, H. 2011, ApJ, 726, 83 (paper II)
- Miyaji, T., Hasinger, G., Salvato, M., et al. 2015, ApJ, 804, 104
- Mountrichas, G. & Georgakakis, A. 2012, MNRAS, 420, 514
- Padmanabhan, N., White, M., Norberg, P., Porciani, C. 2009, MNRAS, 397, 1862
- Planck Collaboration: Ade, P.A.R., Aghanim, N., Arnaud M. 2016, A&A, 2016, 594, A13
- Peebles, P. J. E. 1980, The Large-Scale Structure of the Universe, (Princeton, NJ: Princeton Univ. Press)
- Planck Collaboration XIII, 2016, A&A, 2016, 594, A13
- Powell et al., submitted to ApJ
- Savitzky, A., & Golay, M.J.E. 1964, Anal. Chem., 36, 1627
- Shen, Y., Hennawi, J.F., Shankar, F., et al. 2010, ApJ, 719, 1693
- Shen, Y., Strauss, M.A., Ross, N.P., et al. 2009, ApJ, 697, 1656
- Sheth, R.K., Mo, H.J., & Tormen, G. 2001, MNRAS, 323, 1
- Skibba, R. A., Coil, A. L., Mendez, A. J., et al. 2015, ApJ, 807, 152
- Skrutskie, M.F., Cutri, R.M., Stiening, R., et al. 2006, AJ, 131, 1163
- Tinker, J.L., Weinberg, D.H., Zheng, Z., & Zehavi, I. 2005, ApJ, 631, 41
- Trakhtenbrot, B., Ricci, C., Koss, M.J., et al. 2017, MNRAS, 470, 800
- van den Bosch, F.C. 2002, MNRAS, 331, 98
- Villarroel, B. & Korn, A.J. 2014, NatPh, 10 417
- Worthey, G. 1994, ApJS, 95, 107
- Zhang, S., Wang, T., Wang, H., & Zhou, H. 2013, ApJ, 773, 175
- Zehavi, I., Zheng, Z., Weinberg, D. H., et al. 2005, ApJ, 630, 1
- Zehavi, I., Zheng, Z., Weinberg, D. H., et al. 2010, ApJ, 736, 59
- Zheng, Z., Coil, A. L., & Zehavi, I. 2007, ApJ, 667, 760

This paper has been typeset from a  $\text{\LaTeX}$  file prepared by the author.